Title
Impact of Distinct Origin Locations on the Life Cycles of Landfalling Atmospheric Rivers Over the U.S. West Coast

Journal
Journal of Geophysical Research: Atmospheres, 124(22)

ISSN
2169-897X

Authors
Zhou, Y
Kim, H

Publication Date
2019-11-27

DOI
10.1029/2019JD031218

Peer reviewed

Impact of Distinct Origin Locations on the Life Cycles of Landfalling Atmospheric Rivers over the U.S. West Coast

Yang Zhou[1] and Hyemi Kim[2]

[1]Lawrence Berkeley National Laboratory, Berkeley, CA

[2]School of Marine and Atmospheric Sciences, Stony Brook University, Stony Brook, NY

Corresponding author: Hyemi Kim (hyemi.kim@stonybrook.edu)

Key Points:

- U.S. West Coast landfalling AR events originating from the Northwest Pacific are stronger with longer lifetime than those from the Northeast
- A persistent tripole geopotential height anomaly pattern modulates the life cycles of landfalling AR events from distinct origin locations
- Landfalling AR events originating from the Northwest (Northeast) Pacific induce precipitation over the northern (southern) U.S. West Coast

Abstract

An atmospheric river (AR) event represents strong poleward moisture transport and is defined as a series of spatiotemporally connected instantaneous AR objects. Utilizing an AR tracking algorithm with a depth-first search (a widely-used algorithm in computer science), we examine the life-cycle characteristics of AR events that make landfall over the U.S. West Coast by their distinct origin locations. Landfalling AR events from the Northwest Pacific (120°E-170°W, WLAR events) temporally last longer (5.3 days vs. 3.6 days on average) and have stronger intensity of integrated vapor transport (508 kg m^{-1} s^{-1} vs. 388 kg m^{-1} s^{-1} on average) than those originating from the Northeast Pacific (125°W-170°W, ELAR events). A persistent tripole geopotential height anomaly pattern over the North Pacific modulates the origin locations and propagation of landfalling AR events. WLAR events are associated with anomalous highs over northeastern Asia and the Northeast Pacific and an anomalous low over the central North Pacific. This pattern provides favorable conditions for WLAR events to start, propagate northeastward, and make landfall in the northwestern West Coast. WLAR events contribute approximately 25% of the total winter precipitation over Washington and British Columbia. ELAR events are associated with the nearly opposite tripole pattern to the WLAR events. The anomalous low over the Northeast Pacific helps ELAR events to start, propagate northeastward, and make landfall in the southwestern West Coast. Precipitation induced by ELAR events contributes up to 30% of total winter precipitation over California.

Plain Language Summary

Atmospheric rivers (ARs) are strong poleward water vapor transport events in the lower troposphere. AR events are important to water resources over the U.S. West Coast. We compared the characteristics, circulation patterns, and precipitation of landfalling AR events over the U.S. West Coast based on their origin locations. In general, landfalling AR events originating from the Northwest Pacific (120°E-170°W) last longer and have stronger intensities than those from the Northeast Pacific (125°W-170°W). The life cycles (origin, propagation, and termination) of landfalling AR events and AR-related precipitation are strongly modulated by large-scale tripole geopotential height anomaly pattern over the North Pacific basin.

1 Introduction

Atmospheric rivers (ARs) are filamentary plumes of intensive poleward water vapor transport in the atmosphere that play an essential role in the global hydrological cycle (Zhu & Newell, 1994, 1998). ARs are important to coastal water resources, especially over the U.S. West Coast, where they account for approximately 30-50% of precipitation and snow water equivalent over the region (Dettinger et al., 2011; Guan et al., 2010, 2013; J. Kim et al., 2013; Lavers & Villarini, 2015). About 30-70% of West Coast droughts were ended by AR-related storms (Dettinger, 2013). Strong ARs are associated with heavy precipitation and disastrous events such as floods and extreme winds (Dettinger et al., 2011; Neiman et al., 2013; Ralph et al., 2013; Ralph & Dettinger, 2012; Ralph et al., 2006; Smith et al., 2010; Waliser & Guan, 2017). The number of landfalling ARs and their associated precipitation over the U.S. West Coast are projected to increase with global warming (Dettinger, 2011; Espinoza et al., 2018; Gershunov et al., 2019; Hagos et al., 2016; Lavers et al., 2013; Payne & Magnusdottir, 2015; Warner et al., 2015), which may cause significant economic loss (Dominguez et al., 2018). Therefore, a better understanding of landfalling ARs over the U.S. West Coast and their regional impacts is crucial for accurate predictions and projections of AR-related weather hazards, which could help policymakers and emergency managers to prepare mitigating actions in advance. Given the significant socio-economic impacts of ARs, the characteristics and variability of ARs and the associated physical mechanisms (e.g. Guan & Waliser, 2015; H. Kim et al., 2017; Mundhenk et al., 2016a; Mundhenk et al., 2016b; Payne & Magnusdottir, 2014; Ryoo et al., 2013; Ryoo et al., 2015 and review by Gimeno et al., 2014 and Shields et al., 2018) as well as the prediction of ARs (e.g. DeFlorio et al., 2018a; DeFlorio et al., 2018b; Mundhenk et al., 2018; Nardi et al., 2018; Wick et al., 2013; Zhou & Kim, 2017) have been widely investigated.

Most of the previous studies have focused on the characteristics of landfalling AR events during a relatively short period (about 24-72 hours) during landfall rather than analyzing their entire life cycles from origin to termination (e.g. Neiman et al., 2013; Rutz et al., 2014; Waliser & Guan, 2017). A handful of studies focusing on the entire life cycles of landfalling ARs have been limited to case studies or specific features of AR life cycles, such as intensity or spatial distributions of origin and termination. For example, Ralph et al. (2011) used observational data to track the evolution of a single landfalling AR event over the U.S. West Coast during March 2005 and linked its life cycle with multi-scale dynamical processes such as mesoscale frontal waves and the Madden-Julian Oscillation (MJO). Since this study focused on a single case, it may not represent the general characteristics of the life cycles of landfalling AR events. By focusing on the intensities of landfalling ARs only, Payne and Magnusdottir (2014) showed that stronger landfalling AR events tend to originate from the western Pacific, while the weaker events originate from the eastern Pacific. Sellars et al. (2017) focused on the global distributions of origins and terminations of AR events and the association with climate variability, while other life-cycle characteristics such as lifetime and intensity of ARs were not examined.

In Zhou et al. (2018), an automated object tracking algorithm was developed that can identify the life-cycle characteristics of ARs such as the locations of origin and termination, lifetime, intensity, and the propagation track. While the general characteristics of AR life cycles over the entire North Pacific have been discussed in Zhou et al. (2018), a detailed analysis that specifically targets landfalling AR events over the U.S. West Coast has yet to be conducted. Depending on their origin locations (Northwest (120°E-170°W) vs. Northeast Pacific (125°W-170°W)), landfalling AR events may have distinct characteristics in intensity, propagation pathway, and precipitation location. In this study, the impact of distinct origin locations on the life-cycle characteristics of landfalling AR events over the U.S. West Coast will be examined in detail by adopting the AR tracking algorithm from Zhou et al. (2018). Data selection and the updated tracking algorithm are introduced in section 2. Characteristics of landfalling AR events from different origin locations are compared in section 3. In section 4, we discuss the evolution of landfalling AR events originating from distinct locations and the corresponding large-scale patterns. Spatiotemporal evolution of AR-induced precipitation is examined in section 5. Summary and discussion are provided in section 6.

2 Data and Tracking Algorithm

2.1 Data

To detect ARs, we use the vertically-integrated water vapor transport (IVT), which is calculated as:

$$\mathrm{IVT} = -\frac{1}{g}\int_{1000\,hPa}^{300\,hPa} q\vec{V}\,dp, \quad (1)$$

where g is gravitational acceleration (m s^{-2}), p is pressure (hPa), q is specific humidity (kg kg^{-1}), and $\vec{V}$ is the horizontal wind vector (m s^{-1}). To calculate the IVT, 20 vertical levels (1000-300 hPa) of 6-hourly horizontal winds and specific humidity data from the European Centre for Medium-Range Weather Forecasts Interim Reanalysis (ERAI, (Dee et al., 2011)) are used with 1.0° horizontal grid spacing. To evaluate the evolution of landfalling AR events and circulation patterns, daily (00Z) anomalous (minus daily climatology) horizontal winds, specific humidity, and 500 hPa geopotential height from ERA-Interim are used. To examine the coastal precipitation responses, CPC unified gauge-based analysis of 0.5° daily-mean anomalous precipitation over land (Xie et al., 2007) is analyzed. We focus on 39 cool seasons (1979-2018) from November to March, which is a relatively active season of landfalling ARs (Mundhenk et al., 2016a).

2.2 Tracking Algorithm: Depth-First Search

One of the approaches to detecting ARs is the "condition" parameter detection (Shields et al., 2018), which involves applying a set of conditions on the IVT field at every time step to identify an AR object. The AR object is defined as an enclosed two-dimensional (longitude and latitude) instantaneous area that meets the given AR-related conditions. In this study, we apply the AR detection method developed by Guan and Waliser (2015), who combined multiple conditions including IVT magnitude, IVT direction, and geometric shape. We define an AR event as a series of spatiotemporally connected AR objects. The life cycle of an AR event represents the evolution of multiple overlapping AR objects within an AR event. The AR origin and termination are defined as the first and last AR objects in an AR life cycle, respectively. To identify an AR event and its life cycle, a tracking algorithm was developed in Zhou et al. (2018) that utilizes the spatial overlapping ratio between AR objects of consecutive time steps. An example of an identified landfalling AR event by Zhou et al (2018) is shown in Figure 1. This landfalling AR event originated over the central North Pacific and terminated over the Northwest U.S. during January 2018. The black dots are the centroids of AR objects, which are calculated as the mass-weighted mean latitudes and longitudes of the objects. The letters mark the centroids of origin (O) and termination (T) objects. This landfalling AR event lasted for 4.75 days (19 6-hourly time intervals).

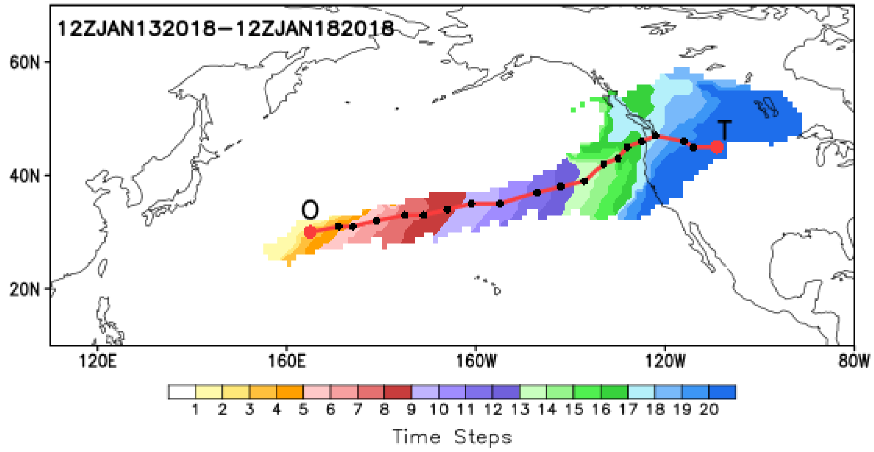

Figure 1. Example of a landfalling AR event (O→T) in January 2018. Each shading color represents an instantaneous AR object from sequential time steps. The black dot marks the centroid of each AR object. The red dots marked with "O" and "T" are the centroids of the origin and termination objects, respectively. The red line connects the dots and represents the propagation track of the landfalling AR event.

When AR objects propagate, it is possible that objects from different AR events merge together or one object splits into multiple objects that propagate in different directions. In Zhou et al (2018), the merging and splitting objects are marked as origins of new AR life cycles. While marking merging and splitting objects as new origins may help to explain the merging or splitting process, the AR events identified in this way may not represent the complete life cycle of moisture transport. To capture the complete life cycles of landfalling AR events, we updated the tracking algorithm from Zhou et al. (2018) so that the merging or splitting objects are identified as intermediate objects rather than new origin objects in AR life cycles. The updated tracking algorithm is based on the tree data structure (Sleator & Tarjan, 1983), which is a widely-used data structure in computer science. The tree data structure contains a set of linked nodes that are distributed hierarchically (Figure 2). Like the shape of a tree, this data structure starts from a root node and moves forward to any linked internal nodes in the next hierarchy. Moving forward, the tree structure may branch out, which means a single internal node is linked to multiple nodes in the next hierarchy. Finally, each branch of the tree structure ends with a terminal node. The life cycle of an AR event is similar to a tree structure. The origin (termination) object is analogous to the root (terminal) node. The merging/splitting object is equivalent to the branching node of the structure. For AR events, the spatiotemporal connectivity (overlapping) is a measure of linkage in the sense of a tree structure, and the number of time steps in the life cycle of an AR event equals the number of hierarchies in a tree structure.

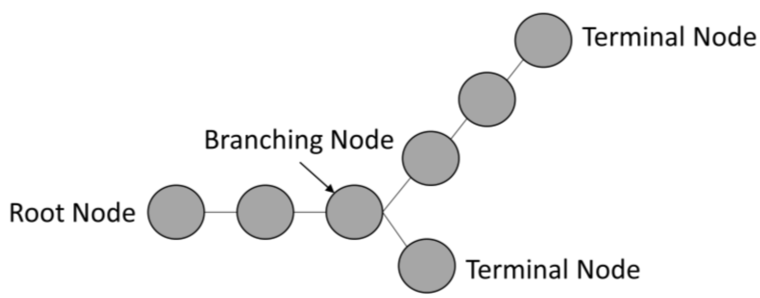

Figure 2. Schematic diagram of a tree structure. This tree structure starts at a root node, branches off, and connects with two terminal nodes.

One of the classic algorithms used to traverse a tree structure is the depth-first search (Tarjan, 1972). The depth-first search algorithm aims to find all the paths between the root node (e.g., AR origin object) and the terminal node (e.g., AR termination object) and to track each branch to the terminal node before moving to the next branch. The updated tracking algorithm applies a depth-first search, which proceeds as follows: i) define the AR origin when an AR object has no overlap with any object in the previous time step (Zhou et al. 2018); ii) starting from the origins, repeatedly find the overlapping object in the next time step until termination (no overlap with the next time step). If a splitting object occurs, each object after the splitting will be tracked separately until termination so that one origin is connected to multiple terminations. If multiple objects merge together, the life cycle after the merging object will be linked to each of the objects before merging so that one termination can be linked to multiple origins. Figure 3 shows an example of two merging AR events during December 2015 identified by the updated tracking algorithm. One AR event originated on December 14 (orange shading, O_1) and the other originated on December 18 (green shading, O_2). The two events merged on December 19 (point M) and terminated (grey shading, T_m) on December 21. The correspondence between one origin and one termination is recorded individually. For instance, the two AR events in Figure 3 are recorded separately ($O_1 \rightarrow T_m$ and $O_2 \rightarrow T_m$), although they have the same termination (T_m). About 28% of total landfalling AR objects are recorded by more than one AR event due to merging and splitting (such as $M \rightarrow T_m$).

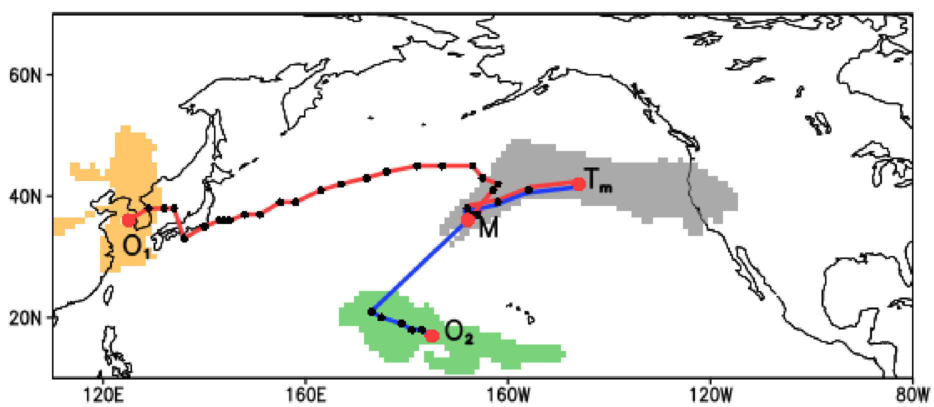

Figure 3. Example of merging AR events during December 2015. The two events originated with different objects (orange (O_1) and green (O_2) shadings), merged, and terminated as the same object (grey shading (T_m)). The red line ($O_1 \rightarrow T_m$) and the blue line ($O_2 \rightarrow T_m$) are the propagation tracks of these two AR events, respectively. "M" marks the time step of merging.

3 Life-Cycle Characteristics by Distinct Origin Locations

We applied the updated algorithm to track landfalling AR events and record their life-cycle characteristics, including the locations of origin and termination, lifetimes, intensities, and propagation tracks. We identified a landfalling AR event as when an AR event has passed through a landfalling region over the U.S. West Coast (blue box in Figure 4a) during its life cycle. The landfalling region is selected along the U.S. West Coast (30°N-49°N) with a zonal width of ten 1° grid points. We tested the sensitivity of landfalling AR events to the landfalling region by zonally shifting the region by three grids or decreasing the zonal width by three grids. The identified landfalling AR events are not sensitive to the width of the landfalling region (not shown). Figure 4a shows the total AR frequency associated with landfalling AR events, which is the grid-point accumulated number of AR objects per winter. AR objects recorded in multiple AR events due to merging/splitting are counted only once in the calculation of AR frequency. The AR frequency spreads over the North Pacific with a maximum of over 45 objects per winter at each grid point between 30°N-60°N adjacent to the West Coast (Figure 4a). On average, about 24 landfalling AR events per winter occur over the U.S. West Coast, which agrees with previous studies (Harris & Carvalho, 2018; Payne & Magnusdottir, 2014). With the tracking algorithm, we can identify the origin and termination objects (Figures 4b-c) from all detected objects associated with landfalling AR events shown in Figure 4a. The AR origin frequency mainly scatters between 20°N-45°N in the North Pacific, with the maximum frequency over the subtropical Northeast Pacific. A secondary peak in origin frequency locates over the Northwest Pacific near 160°E, which suggests that a large number of landfalling AR events originate from the Northwest Pacific, travel across the North Pacific basin, and make landfall over the U.S. West Coast. The high termination frequency over land is due to the massive moisture loss through precipitation when ARs make landfall (Dettinger, 2013; Neiman et al., 2013; Ralph & Dettinger, 2012).

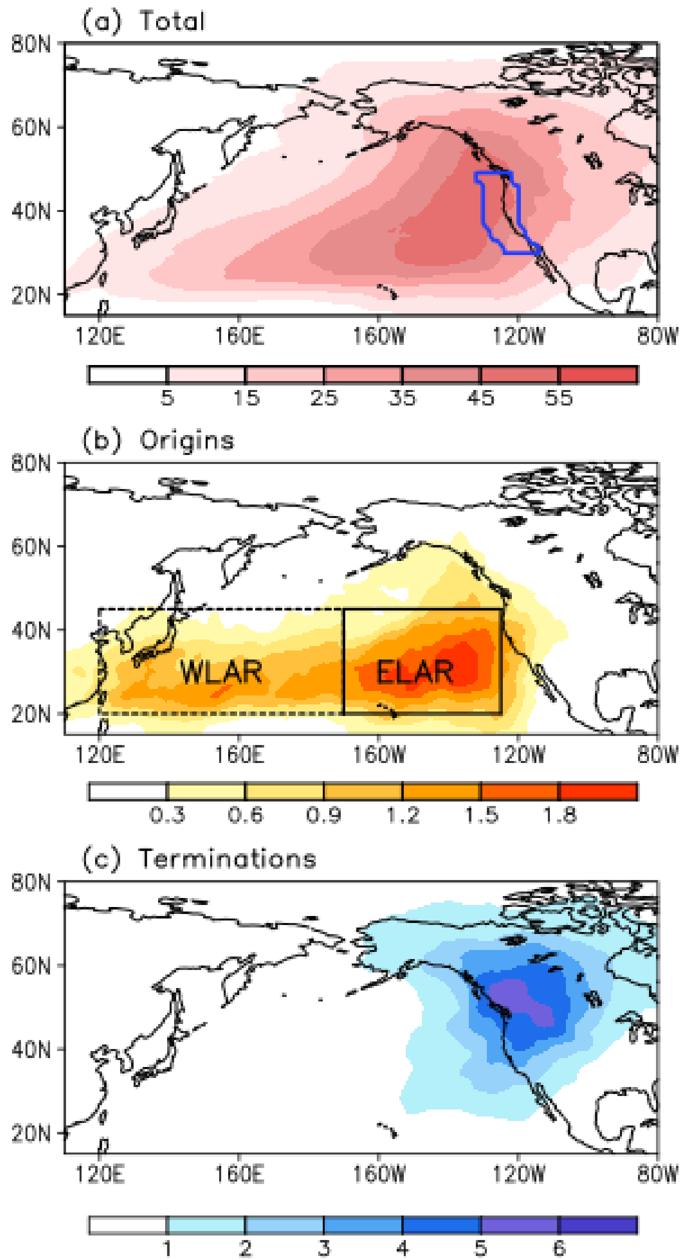

Figure 4. AR frequency (shading, number of objects per winter) for (a) total, (b) origin, and (c) termination objects in landfalling AR events. The area enclosed by the blue line in (a) is the region for landfalling AR event selection (10 longitudinal degrees along the U.S. West Coast between 30°N-49°N). Boxes in (b) denote the origin locations of landfalling AR events from the

Northwest Pacific (20°N-45°N, 120°E-170°W) (WLAR, dashed box) and landfalling AR events from the Northeast Pacific (20°N-45°N, 125°W-170°W) (ELAR, solid box).

To compare the characteristics of landfalling AR events from different origin locations, we categorized the landfalling AR events into two groups based on their origin locations: landfalling AR events from the Northwest Pacific (WLAR events, dashed box in Figure 4b) and the Northeast Pacific (ELAR events, solid box in Figure 4b). To determine the domain for event selection, empirical orthogonal function (EOF) is applied to daily anomalous AR frequency (20°N-60°N, 120°E-250°E) that are associated with landfalling AR events. To calculate daily anomalous AR frequency, we first summed the objects associated with landfalling AR events by every four 6-hourly time steps, then subtracted the daily climatology. Figure 5 shows the first two EOF modes. The first mode (12.5% variance explained) is a basin-scale monopole pattern of daily AR frequency over the entire North Pacific, which reflects the occurrence location of landfalling AR objects (Figure 5a). The second mode (8.9% variance explained) shows a west-east dipole pattern with the maxima over the Northeast Pacific around 30°N, 135°W and the minima over the central Pacific near 40°N, 160°W (Figure 5b). The second EOF mode could explain the variability of landfalling AR events from the Northeast Pacific (125°W-170°W) and from the Northwest Pacific (120°E-170°W). Therefore, we selected the two domains of origin locations based on the distinct west-east variation of daily AR frequency of landfalling AR events (Figure 4b). For 39 cool seasons, a total of 438 WLAR events and 499 ELAR events are selected for detailed analysis of landfalling AR life cycles.

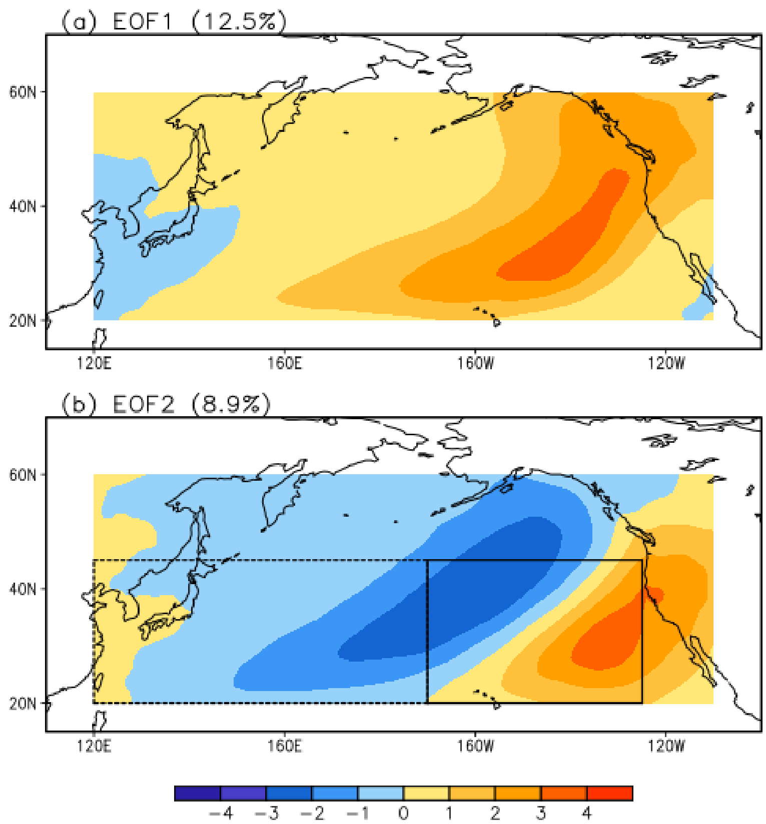

Figure 5. Spatial patterns of (a) the first and (b) second EOF modes of daily AR frequency associated with landfalling AR events. The black boxes in (b) are the same as Figure 4(b) which mark the selection domains for AR origins. The percentage shown in each panel's title represents the variance explained by each mode.

The lifetime of an AR event is calculated as the product of the number of time intervals between origin and termination, and the length of the time interval (6 hours). For example, the lifetime of the landfalling AR event shown in Figure 1 is 4.75 days. Figure 6a shows the probability density function (PDF) of the lifetimes of WLAR and ELAR events. For ELAR events, the percentage gradually decreases as a function of lifetime. About 77% of ELAR events' lifetimes persist less than 4 days (Figure 6a). We examined the ELAR events in the high tail of the distribution (lifetime > 5.5 days, ~85th percentile) and found that the prolonged lifetimes of those ELAR events are due to slow-moving AR objects or merging with other AR events (not shown). The mean lifetime of ELAR events is 3.6 days, which is different from that of WLAR events (5.3 days) on a 99% confidence level based on a two-sample t-test. About 60% of WLAR events have lifetimes longer than 4 days because it requires more time for WLAR events to travel across the North Pacific basin and reach the West Coast. The shorter-lived WLAR events (< 2.5 days, ~15th percentile) mostly have origins closer to the central Pacific (not shown) and longer-lived WLAR events (> 7 days, ~85th percentile) originate further west.

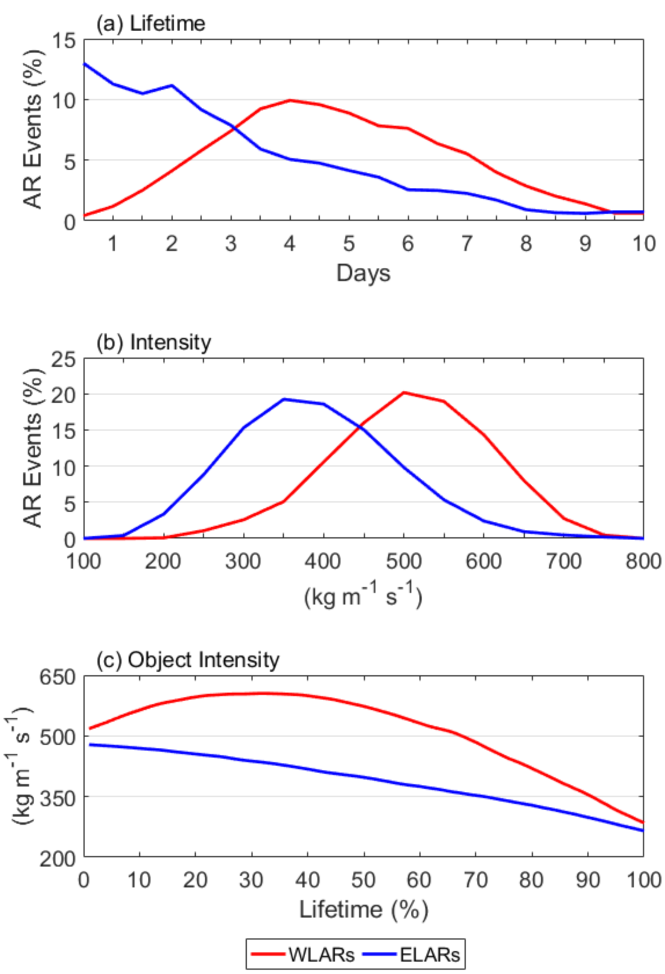

Figure 6. PDF of (a) lifetime (days), (b) mean intensity (kg m^{-1} s^{-1}), and (c) change of object intensity through the lifetime (percentage of lifetime) for WLAR (red) and ELAR (blue) events.

The intensity of an AR event is calculated as the average of objects' intensities which are the area-weighted mean IVT magnitudes within the AR objects. Figure 6b shows the PDF of the intensities of WLAR and ELAR events. The mean intensity is 508 kg m^{-1} s^{-1} for WLAR events and 388 kg m^{-1} s^{-1} for ELAR events, which are significantly different on a 99% confidence level based on a two-sample t-test. A previous study also showed that AR events originating from the western Pacific generally have stronger intensities than those from the eastern Pacific (Payne & Magnusdottir, 2014). To further understand why WLAR events have stronger intensities than ELAR events, we investigated the intensity changes during landfalling AR life cycles. Because the lengths of lifetimes vary among landfalling AR events (Figure 6a), we interpolated the time series of object intensity into 100 portions for every landfalling AR event for easier comparison. 0% represents the origin and 100% represents the termination. For example, in Figure 1, 40% of the lifetime represents the first 1.9 days of the total 4.75 days. Figure 6c shows the temporal change in the object intensity of WLAR and ELAR events. WLAR events on average have stronger object intensity than ELAR events throughout their life cycles. The mean object intensity continuously decreases in ELAR events, whereas it increases during the first 20% of the lifetime and then gradually decreases for WLAR events (Figure 6c).

4 Distinct Evolutions of Landfalling AR Events

To better understand the evolutions of landfalling AR events, we calculated the daily AR frequency starting from origins (Day +0) (Figure 7). Since the AR origins can occur in any of the four 6-hourly time steps during Day +0, we included the origin objects from all four time steps for Day +0 in Figure 7. After Day +0, only the AR objects at 00z are used and referred to as daily for simplicity. A three-day (i.e., three 00z) moving average is performed after Day +0. For example, Day +2 represents the average from Days +1 to +3.

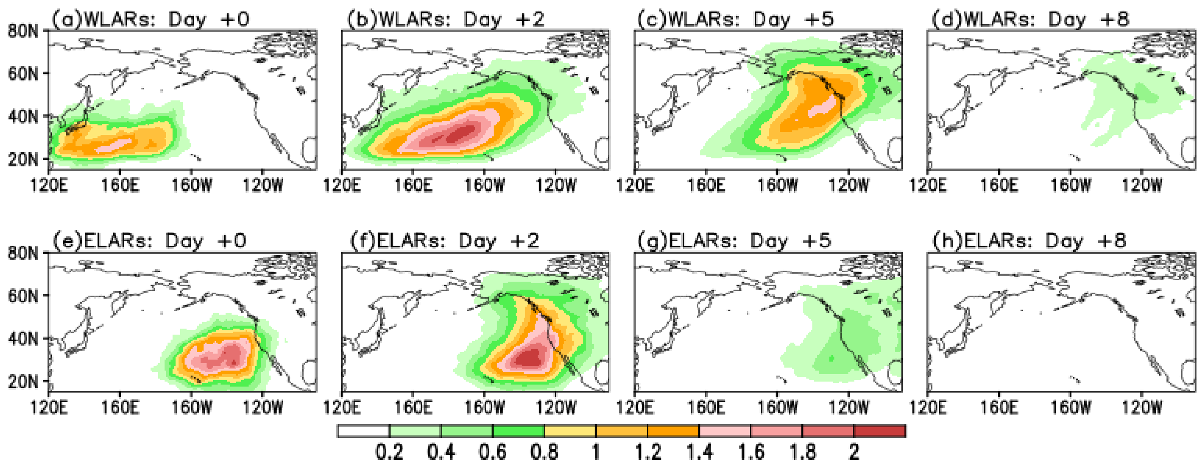

Figure 7. AR frequency (number of objects per winter) of (a-d) WLAR and (e-h) ELAR events from Day +0 to Day +8. A three-day moving average is applied except for Day +0.

On Day +0, the origin objects of 438 WLAR events spread over the subtropical Northwest Pacific with a maximum (over 1.4 objects per winter) between 20°N-30°N, 140°E-170°E (Figure 7a). On Day +2, as objects of WLAR events propagate northeastward, the area covered by WLAR objects enlarges over the North Pacific, with the maximum (over 2 objects per winter) in the subtropical central Pacific (Figure 7b). The broad area of WLAR frequency may be due to various propagation directions of WLAR events or intensification of WLAR events as shown in Figure 6c. A few WLAR events make landfall over the West Coast on Day +2 with less than 0.6 objects per winter over grid points in western North America (Figure 7b). After Day +2, the overall WLAR frequency decreases due to the weakening of intensity (Figure 6c) or increasing number of terminated events. Day +5 is the peak landfall period for WLAR events with over 0.8 object per winter between 40°N-70°N and roughly 1.4 objects per winter near 50°N (Figure 7c). About 15% of all WLAR events last longer than 7 days and make landfall on Day +8 (Figure 6a and 7d). The landfalling latitudes of WLAR events are generally in the northwestern U.S. West Coast and British Columbia. Because ELAR events originate geographically closer to the U.S. West Coast, some ELAR events already extend to the West Coast on Day +0 with the maximum frequency of 1 object per winter over the grids near 35°N (Figure 7e). The ELAR frequency expands northward and reaches 70°N on Day +2 (Figure 7f). Day +2 is the peak landfall period for ELAR events. The ELAR frequency over the entire North American West Coast (25°N-60°N) is over 0.2 object per grid per winter, with a maximum of 1.6 objects per winter near 35°N (Figure 7f). After the peak of landfall, the ELAR frequency decreases rapidly (Figures 7g-h).

To understand the evolution processes and large-scale patterns associated with the landfalling AR events, we calculated the composites of anomalous geopotential height at 500 hPa (Z500), IVT, and moisture flux divergence from six days prior (Day –6) to nine days after (Day +9) landfalling AR origins (Figures 8 and 9). The selected time steps in Figures 8 and 9 are consistent with landfalling AR events shown in Figure 7. A three-day moving average is applied to the anomalous fields except for Day +0. For example, Day –5 represents the average of Day –6 to –4. For the significance test, a one-sample t-test is applied to the anomalous fields on each composite day. The significant values shown in Figure 8 and 9 represent that the value over the grid is 95% significantly different from the climatology for at least one day among the three-day averaging.

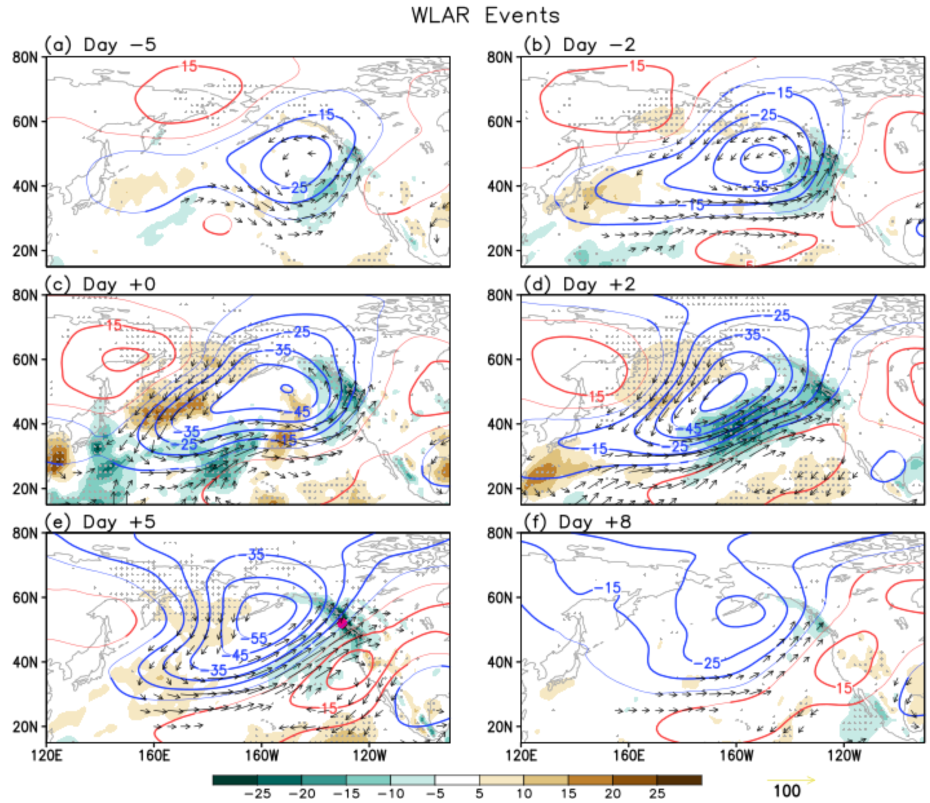

Figure 8. Daily composites of anomalous Z500 (contours, 10-meter interval, zero line is omitted, red/blue contours represent positive/negative anomalies), IVT anomaly (vectors larger than 15 kg m^{-1} s^{-1}), and anomalous moisture flux divergence (shading, 1×10^{7} kg m^{-1} s^{-1} interval) for WLAR events. A three-day moving average is applied except for Day +0. The magenta dot in (e) marks the location of maximum frequency during landfall. The dotted shading, thickened contours, and vectors represent values that exceed the 95% confidence level of a one-sample t-test.

The life cycles of WLAR events are associated with a tripole pattern of geopotential height anomalies over the North Pacific that persists for one week (from Day –2 to +5) with an anomalous low over the central North Pacific and anomalous highs over northeast Asia and the subtropical Northeast Pacific (Figure 8). A similar tripole pattern associated with landfalling ARs over Oregon is shown in Benedict et al. (2019) by calculating lagged regression of geopotential height onto the IVT at landfall. On Day –5, an anomalous high appears over northeastern Asia and an anomalous low emerges over the North Pacific (Figure 8a). As the two height anomalies intensify from Day –5 to +0, the increasing pressure gradient induces an equatorward IVT anomaly and enhanced moisture flux divergence at the northwest side of the anomalous low (Figures 8a-c). The equatorward IVT decays from Days +2 to +8 with the weakening anomalous high over northeastern Asia (Figures 8d-f). Another anomalous high intensifies over the Northeast Pacific from Days –2 to +5. Meanwhile, an eastward IVT anomaly and enhanced moisture flux convergence prevail between the anomalous low and high due to an increased pressure gradient (Figures 8b-e). The combination of the anomalous low and high modulates the origin and propagation of WLAR events. The eastward IVT anomaly supports the occurrence of WLAR origins on Day +0. Anomalous moisture flux convergence is induced over the Northwest U.S. and British Columbia during the landfall of WLAR events and persists until this tripole Z500 anomaly pattern dissipates on Day +5 (Figures 8d-f).

A similar tripole pattern is shown associated with ELAR events but shifted eastward comparing to WLAR events (Figure 9). An anomalous high, which induces an anticyclonic circulation, persists over the northwestern Pacific from Days –5 to +2. Correspondingly, equatorward (poleward) IVT and enhanced moisture flux divergence (convergence) remain at the east (west) side of the anomalous high from Days –5 to +2 (Figures 9a-d). On Day –2, an anomalous low, which modulates the occurrence and propagation of ELAR events, prevails over the Northeast Pacific (Figure 9b). As the anomalous low deepens, the IVT magnitude increases (not shown) and therefore leads to the origin of ELAR events (Figure 9c). On Day +0, another anomalous high appears over western Mexico. This anomalous high develops from Day +0 to +2 and dissipates after Day +2 (Figures 9c-f). The northward steering flow between the anomalous low and high over the Northeast Pacific may be associated with the spread of landfalling latitudes of ELAR events (Figure 9f). The maximum moisture flux convergence which is associated with the landfalls of ELAR events appears further south compared to that of WLAR events. The tripole anomalous Z500 pattern related to ELAR events persists for about one week and gradually dissipates after Day +5 (Figures 9e-f) as ELAR events terminate (Figures 7g).

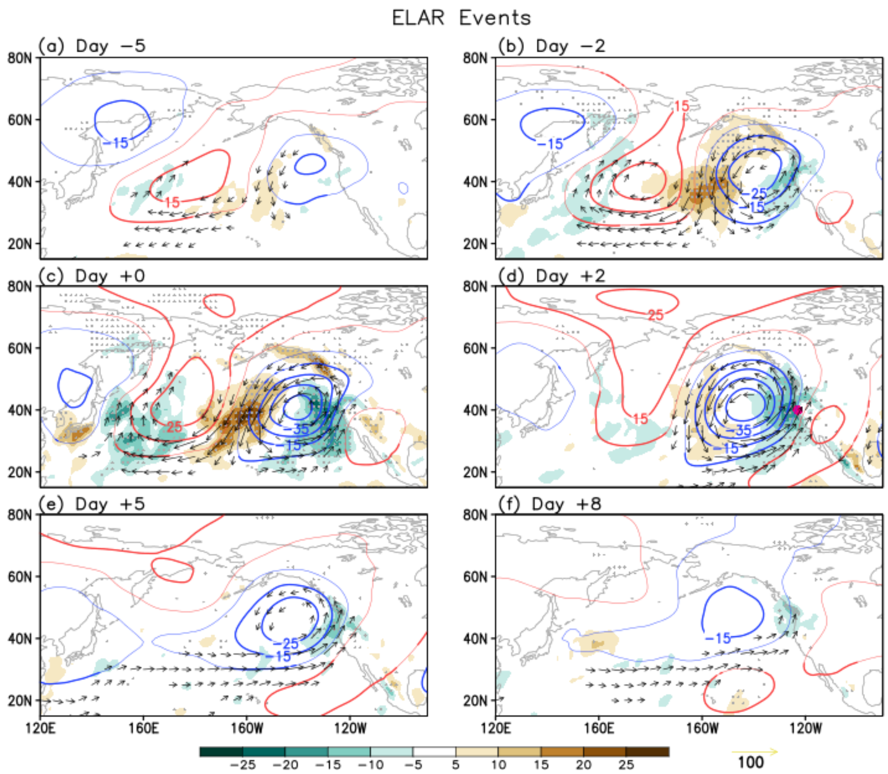

Figure 9. Same as Figure 8 but for ELAR events. The magenta dot in (d) marks the location of maximum frequency during landfall.

5 AR-Induced Precipitation

To examine the precipitation related to WLAR and ELAR events, percentages of AR-induced precipitation over the West Coast are calculated (Figure 10). We summed the daily precipitation over 39 winters when an AR object made landfall and divided it by the total winter precipitation accumulated over 39 winters. On average, about 40% of winter precipitation is sourced from landfalling ARs over the West Coast, which is consistent with previous studies (Dettinger et al., 2011; Gershunov et al., 2017; Guan et al., 2010, 2013; J. Kim et al., 2013). The precipitation contributed by WLAR and ELAR events is compared in Figure 10. The percentage of WLAR-induced precipitation increases from south to north, with about 10% in Southern California, 10-20% in Northern California and Oregon, and 20-30% in British Columbia and Washington (Figure 10a). The higher percentages (over 20%) between 45°N-60°N match well with the area of enhanced moisture flux convergence and landfall latitudes (Figures 8d-e). The percentage of precipitation induced by ELARs is about 30% over California, 20-30% over Oregon and Washington, and 15-20% over British Columbia (Figure 10b). Overall, total winter precipitation induced by ELAR events is higher than that by WLAR events, possibly due to the ELAR events occurs more frequently in total (Figures 7).

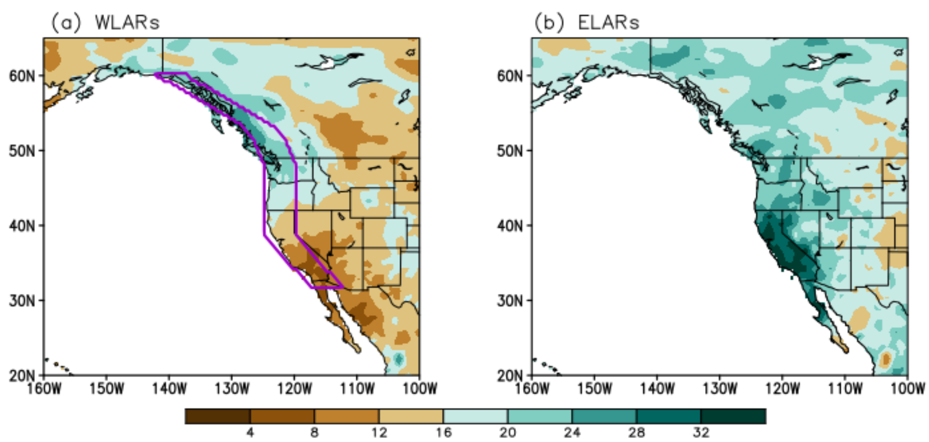

Figure 10. Percentage (%) of AR-induced precipitation to total winter precipitation by (a) WLAR and (b) ELAR events. The region with a width of five longitudinal degrees (10 grids in 0.5°) along the West Coast from 32°N-60°N (marked with the purple polygon in (a)) shows the region for the zonal average shown in Figure 11.

To further understand the temporal changes of AR-induced precipitation, we calculated the temporal evolution (starting from AR origins) of the AR-induced precipitation anomaly (Figure 11, mm per event) zonally-averaged over the U.S. West Coast (enclosed purple polygon in Figure 10a). The x-axis labels in Figure 11 are consistent with the subplot titles in Figures 7-9 where Day +0 represents the day of AR origin. A three-day moving average is also applied after Day +0 in Figure 11. During the life cycle of every AR event, we include daily mean precipitation only when an AR object is over land during the 10-day period. Since AR conditions can persist for 24hr to 120hr after landfall (Payne & Magnusdottir, 2016; Ralph et al., 2013; Ralph et al., 2011; Ralph et al., 2019), the precipitation caused by one landfalling AR event will be counted in multiple consecutive days as long as the AR condition persists after landfall.

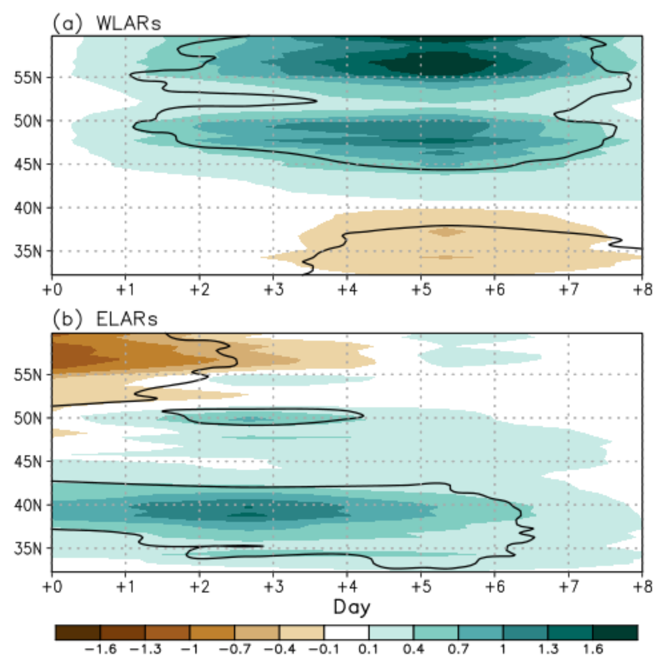

Figure 11. Evolution of AR-induced precipitation anomalies (shading, mm per event) averaged along the West Coast (enclosed red polygon in Figure 10a) for (a) WLAR and (b) ELAR events. Day +0 represents the AR origin. The areas enclosed by black contours are statistically

significant at the 95% confidence level based on a one-sample t-test. A three-day moving average is applied, except for Day +0.

For WLAR events, the increased AR-induced precipitation persists between 40°N-60°N from Days +2 to +8 with the maximum increase of over 2 mm per event between 55°N-60°N on Day +5 (Figure 11a). The increased precipitation on Day +2 corresponds with the enhanced moisture flux convergence induced by the anomalous low over the North Pacific (Figure 8d). The positive precipitation anomalies on Day +5 match with the peak of landfalling WLAR events (Figure 8e). Meanwhile, the reduced precipitation over the southern West Coast from Days +2 to +8 is associated with the enhanced moisture flux divergence between 20°N-40°N accompanied by the anomalous high over the Northeast Pacific (Figures 8d-f).

Positive precipitation anomalies appear between 35°N-45°N on Day +0 (Figure 11b) because some ELAR events reach the West Coast during their origins (Figure 7e). The positive precipitation anomalies last until Day +8 with a maximum increase of 1.3 mm per event between 35°N-40°N on Days +2, which match with the peak landfall period of ELAR events (Figure 7f). The positive precipitation anomalies weaken after Day +2 due to the increasing number of terminated ELAR events (Figures 7g-h). The continuous positive precipitation anomalies from Days +5 to +8 may be due to persistent moisture support from the tropics or merging of events, which prolongs the lifetimes of ELAR events (long tail in Figure 6a). Meanwhile, negative precipitation anomalies appear between 50°N-60°N from Days +0 to +2, which is related to the moisture flux divergence anomaly associated with the anomalous high over the central North Pacific (Figures 9c-d).

6 Summary and Discussion

To understand the impacts of distinct origin locations on the life cycles of AR events that make landfall over the U.S. West Coast, we investigated the landfalling AR events originating from the Northwest and Northeast Pacific by examining their life-cycle characteristics, associated circulation patterns, and precipitation anomalies during 39 winters from 1979 to 2018. We applied an AR tracking algorithm using a depth-first search to identify the life cycles of landfalling AR events. Generally, WLAR events are prone to landfall in the Northwest U.S. and British Columbia, while ELAR events have a vast range of landfalling latitudes along the U.S. West Coast. WLAR events have longer lifetimes and stronger intensities than ELAR events.

Two schematic diagrams are shown in Figure 12 to describe the distinct life cycles of WLAR and ELAR events. WLAR events are induced by northeastward IVT anomalies at the southeast side of the cyclonic circulation associated with an anomalous low over the central North Pacific (Figure 12a). Within 4-5 days after WLAR origins, maximum precipitation appears over the northern West Coast associated with the landfalls of WLAR events. The accumulated precipitation induced by WLAR events contributes 20-25% of the total winter precipitation over British Columbia and Washington. On the other hand, reduced precipitation occurs over the southern West Coast due to reduced moisture flux convergence associated with the anticyclonic flow anomaly over the Northeast Pacific. Such tripole pattern that shifts eastward is linked to the occurrence and propagation of ELAR events (Figure 12b). The anomalous low over the Northeast Pacific accelerates the cyclonic circulation, which enhances the northeastward IVT, triggers ELAR events, and supports their northeastward propagation. The ELAR events lead to maximum precipitation over the southern West Coast approximately 2 days after their origins. ELAR-induced precipitation produces up to 30% of total winter precipitation over California.

Meanwhile, reduced precipitation over the northern West Coast is attributed to the moisture flux divergence anomaly. While previous work has shown the large-scale patterns associated with precipitation over the west coast of North America (Benedict et al., 2019; Carrera et al., 2004; Higgins et al., 2000; Jiang & Deng, 2011; Lackmann & Gyakum, 1999), our study further demonstrates that the life cycle of AR events can serve as an indicator to show how the large-scale patterns modulate the pathway of moisture transport prior to the precipitation over land.

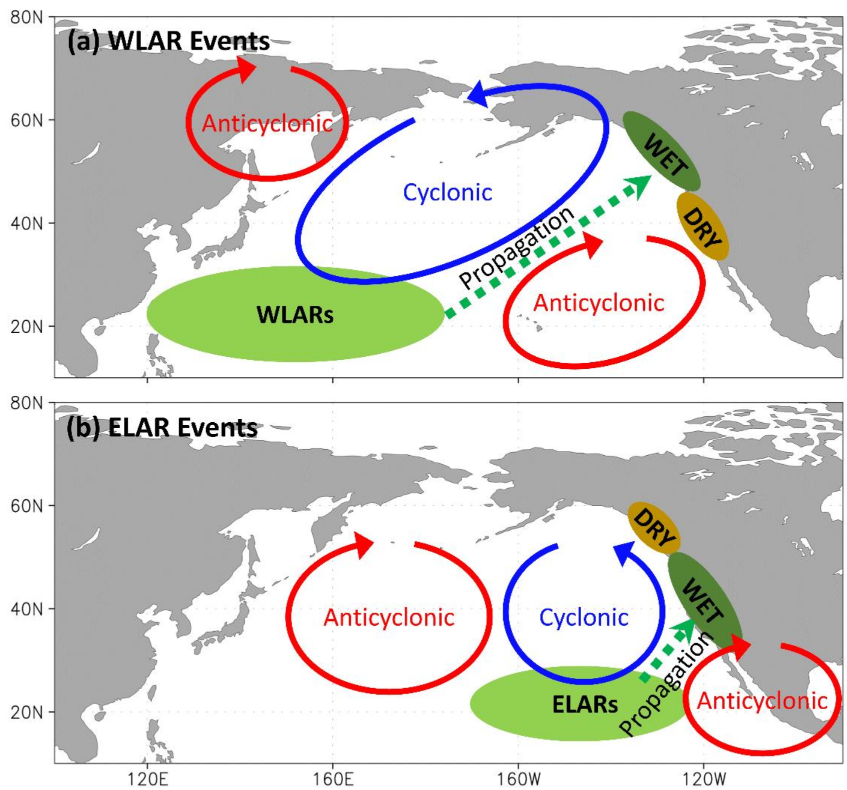

Figure 12. Schematic diagrams for the large-scale patterns, evolutions, and precipitation anomalies related to the life cycles of (a) WLAR and (b) ELAR events. Green ovals mark the distinct origin locations. Dashed green arrows indicate the propagation direction of AR events. Circle arrows denote the circulation direction where the blue (red) arrow indicates cyclonic (anticyclonic) circulation. Green and brown colors represent wet and dry precipitation anomalies, respectively.

Our results indicate that the life cycles of AR events can be useful tools to improve the forecasts of ARs and associated precipitation over the West Coast. With the empirical relationships discussed in this study, it may be possible to forecast the propagation track, termination location, and precipitation amount associated with a specific AR by knowing its origin location. In addition, since the signal of the tripole Z500 anomaly pattern occurs approximately 5 days prior to AR origins and persists for a week, the circulation patterns can be considered as potential precursors for landfalling AR events and therefore may help improve the subseasonal prediction of landfalling AR activity.

Recently, research interest has been growing in the subseasonal prediction of ARs because the subseasonal forecast is particularly important in making management decisions regarding water, agriculture, and hazards. Skillful prediction of weekly AR occurrence is maintained for up to 3 weeks (DeFlorio et al., 2018b) and can be further extended to 5 weeks by taking the MJO and Quasi-Biennial Oscillation into account (Baggett et al., 2017; Mundhenk et al., 2018). The MJO is a major source of subseasonal predictability for ARs because the MJO-induced tropical heating can modulate ARs by perturbing midlatitude geopotential heights via Rossby wave teleconnections (Guan et al., 2012; Payne & Magnusdottir, 2014; Ralph et al., 2011; Stan et al., 2017). Therefore, to further improve subseasonal AR prediction, it is crucial to understand the physical processes governing the MJO's modulation of ARs. The AR life cycle approach may help to extend the understanding of how the MJO influences AR activity by linking the spatiotemporal evolution of AR events to the propagation of the MJO. For example, by comparing the life cycles of AR events during different MJO phases, it is feasible to study the dynamical mechanisms of how the MJO's intensity, propagation, and teleconnection patterns modulate the origin locations and evolutions of AR events, which has implications for a better understanding of AR activity and improving the subseasonal AR prediction.

Acknowledgment

Constructive and valuable comments from three anonymous reviewers are greatly appreciated. YZ was supported by NSF grant AGS-1652289 and by the U.S. Department of Energy, Office of Science, Office of Biological and Environmental Research, Climate and Environmental Sciences Division, Regional & Global Climate Modeling Program, under Award Number DE-AC02-05CH11231. HK was supported by NSF grant AGS-1652289 and the KMA R&D Program grant KMI2018-03110. The sources of data used in this study are: http://apps.ecmwf.int/datasets/data/interim-full-daily/levtype=pl/ for ERA-Interim reanalysis; https://www.esrl.noaa.gov/psd/data/gridded/data.cpc.globalprecip.html for CPC Global Unified Gauge-Based Analysis of Daily Precipitation.

Reference

Baggett, C. F., Barnes, E. A., Maloney, E. D., & Mundhenk, B. D. (2017). Advancing atmospheric river forecasts into subseasonal-to-seasonal time scales. *Geophysical Research Letters, 44*(14), 7528-7536. doi:10.1002/2017gl074434

Benedict, J. J., Clement, A. C., & Medeiros, B. (2019). Atmospheric blocking and other large-scale precursor patterns of landfalling atmospheric rivers in the North Pacific: A CESM2 study. *Journal of Geophysical Research: Atmospheres, 0*(ja). doi:10.1029/2019jd030790

Carrera, M. L., Higgins, R. W., & Kousky, V. E. (2004). Downstream weather impacts associated with atmospheric blocking over the northeast Pacific. *Journal of Climate, 17*(24), 4823-4839. doi:10.1175/Jcli-3237.1

Dee, D. P., Uppala, S. M., Simmons, A. J., Berrisford, P., Poli, P., Kobayashi, S., et al. (2011). The ERA-Interim reanalysis: configuration and performance of the data assimilation system. *Quarterly Journal of the Royal Meteorological Society, 137*(656), 553-597. doi:10.1002/qj.828

DeFlorio, M. J., Waliser, D. E., Guan, B., Lavers, D. A., Ralph, F. M., & Vitart, F. (2018a). Global Assessment of Atmospheric River Prediction Skill. *Journal of Hydrometeorology, 19*(2), 409-426. doi:10.1175/Jhm-D-17-0135.1

DeFlorio, M. J., Waliser, D. E., Guan, B., Ralph, F. M., & Vitart, F. (2018b). Global evaluation of atmospheric river subseasonal prediction skill. *Climate Dynamics*. doi:10.1007/s00382-018-4309-x

Dettinger, M. D. (2011). Climate Change, Atmospheric Rivers, and Floods in California - A Multimodel Analysis of Storm Frequency and Magnitude Changes. *Journal of the*

American Water Resources Association, 47(3), 514-523. doi:10.1111/j.1752-1688.2011.00546.x

Dettinger, M. D. (2013). Atmospheric Rivers as Drought Busters on the US West Coast. *Journal of Hydrometeorology, 14*(6), 1721-1732. doi:10.1175/Jhm-D-13-02.1

Dettinger, M. D., Ralph, F. M., Das, T., Neiman, P. J., & Cayan, D. R. (2011). Atmospheric Rivers, Floods and the Water Resources of California. *Water, 3*(2), 445-478. doi:10.3390/w3020445

Dominguez, F., Dall'erba, S., Huang, S., Avelino, A., Mehran, A., Hu, H., et al. (2018). Tracking an atmospheric river in a warmer climate: from water vapor to economic impacts. *Earth Syst. Dynam., 9*(1), 249-266. doi:10.5194/esd-9-249-2018

Espinoza, V., Waliser, D. E., Guan, B., Lavers, D. A., & Ralph, F. M. (2018). Global Analysis of Climate Change Projection Effects on Atmospheric Rivers. *Geophysical Research Letters, 45*(9), 4299-4308. doi:10.1029/2017gl076968

Gershunov, A., Shulgina, T., Clemesha, R. E. S., Guirguis, K., Pierce, D. W., Dettinger, M. D., et al. (2019). Precipitation regime change in Western North America: The role of Atmospheric Rivers. *Scientific Reports, 9*. doi:ARTN 994410.1038/s41598-019-46169-w

Gershunov, A., Shulgina, T., Ralph, F. M., Lavers, D. A., & Rutz, J. J. (2017). Assessing the climate-scale variability of atmospheric rivers affecting western North America. *Geophysical Research Letters, 44*(15), 7900-7908. doi:10.1002/2017gl074175

Gimeno, L., Nieto, R., Vazquez, M., & Lavers, D. A. (2014). Atmospheric rivers: a mini-review. *Frontiers in Earth Science, 2*(2). doi:10.3389/feart.2014.00002

Guan, B., Molotch, N. P., Waliser, D. E., Fetzer, E. J., & Neiman, P. J. (2010). Extreme snowfall events linked to atmospheric rivers and surface air temperature via satellite measurements. *Geophysical Research Letters, 37*. doi:Artn L2040110.1029/2010gl044696

Guan, B., Molotch, N. P., Waliser, D. E., Fetzer, E. J., & Neiman, P. J. (2013). The 2010/2011 snow season in California's Sierra Nevada: Role of atmospheric rivers and modes of large-scale variability. *Water Resources Research, 49*(10), 6731-6743. doi:10.1002/wrcr.20537

Guan, B., & Waliser, D. E. (2015). Detection of atmospheric rivers: Evaluation and application of an algorithm for global studies. *Journal of Geophysical Research-Atmospheres, 120*(24), 12514-12535. doi:10.1002/2015jd024257

Guan, B., Waliser, D. E., Molotch, N. P., Fetzer, E. J., & Neiman, P. J. (2012). Does the Madden–Julian Oscillation Influence Wintertime Atmospheric Rivers and Snowpack in the Sierra Nevada? *Monthly Weather Review, 140*(2), 325-342. doi:10.1175/mwr-d-11-00087.1

Hagos, S. M., Leung, L. R., Yoon, J. H., Lu, J., & Gao, Y. (2016). A projection of changes in landfalling atmospheric river frequency and extreme precipitation over western North America from the Large Ensemble CESM simulations. *Geophysical Research Letters, 43*(3), 1357-1363. doi:10.1002/2015gl067392

Harris, S. M., & Carvalho, L. M. V. (2018). Characteristics of southern California atmospheric rivers. *Theoretical and Applied Climatology, 132*(3-4), 965-981. doi:10.1007/s00704-017-2138-1

Higgins, R. W., Schemm, J. K. E., Shi, W., & Leetmaa, A. (2000). Extreme precipitation events in the western United States related to tropical forcing. *Journal of Climate, 13*(4), 793-820. doi:10.1175/1520-0442(2000)013<0793:Epeitw>2.0.Co;2

Jiang, T. Y., & Deng, Y. (2011). Downstream modulation of North Pacific atmospheric river activity by East Asian cold surges. *Geophysical Research Letters, 38*(20), n/a-n/a. doi:Artn L2080710.1029/2011gl049462

Kim, H., Zhou, Y., & Alexander, M. A. (2017). Changes in atmospheric rivers and moisture transport over the Northeast Pacific and western North America in response to ENSO diversity. *Climate Dynamics*, 1-14. doi:10.1007/s00382-017-3598-9

Kim, J., Waliser, D. E., Neiman, P. J., Guan, B., Ryoo, J. M., & Wick, G. A. (2013). Effects of atmospheric river landfalls on the cold season precipitation in California. *Climate Dynamics, 40*(1-2), 465-474. doi:10.1007/s00382-012-1322-3

Lackmann, G. M., & Gyakum, J. R. (1999). Heavy Cold-Season Precipitation in the Northwestern United States: Synoptic Climatology and an Analysis of the Flood of 17–18 January 1986. *Weather and Forecasting, 14*(5), 687-700. doi:10.1175/1520-0434(1999)014<0687:hcspit>2.0.co;2

Lavers, D. A., Allan, R. P., Villarini, G., Lloyd-Hughes, B., Brayshaw, D. J., & Wade, A. J. (2013). Future changes in atmospheric rivers and their implications for winter flooding in Britain. *Environmental Research Letters, 8*(3). doi:Artn 03401010.1088/1748-9326/8/3/034010

Lavers, D. A., & Villarini, G. (2015). The contribution of atmospheric rivers to precipitation in Europe and the United States. *Journal of Hydrology, 522*, 382-390. doi:10.1016/j.jhydrol.2014.12.010

Mundhenk, B. D., Barnes, E. A., & Maloney, E. D. (2016a). All-Season Climatology and Variability of Atmospheric River Frequencies over the North Pacific. *Journal of Climate, 29*(13), 4885-4903. doi:10.1175/Jcli-D-15-0655.1

Mundhenk, B. D., Barnes, E. A., Maloney, E. D., & Baggett, C. F. (2018). Skillful empirical subseasonal prediction of landfalling atmospheric river activity using the Madden–Julian oscillation and quasi-biennial oscillation. *npj Climate and Atmospheric Science, 1*(1), 20177. doi:10.1038/s41612-017-0008-2

Mundhenk, B. D., Barnes, E. A., Maloney, E. D., & Nardi, K. M. (2016b). Modulation of atmospheric rivers near Alaska and the US West Coast by northeast Pacific height anomalies. *Journal of Geophysical Research-Atmospheres, 121*(21), 12751-12765. doi:10.1002/2016jd025350

Nardi, K. M., Barnes, E. A., & Ralph, F. M. (2018). Assessment of Numerical Weather Prediction Model Reforecasts of the Occurrence, Intensity, and Location of Atmospheric Rivers along the West Coast of North America. *Monthly Weather Review, 146*(10), 3343-3362. doi:10.1175/Mwr-D-18-0060.1

Neiman, P. J., Ralph, F. M., Moore, B. J., Hughes, M., Mahoney, K. M., Cordeira, J. M., & Dettinger, M. D. (2013). The Landfall and Inland Penetration of a Flood-Producing Atmospheric River in Arizona. Part I: Observed Synoptic-Scale, Orographic, and Hydrometeorological Characteristics. *Journal of Hydrometeorology, 14*(2), 460-484. doi:10.1175/Jhm-D-12-0101.1

Payne, A. E., & Magnusdottir, G. (2014). Dynamics of Landfalling Atmospheric Rivers over the North Pacific in 30 Years of MERRA Reanalysis. *Journal of Climate, 27*(18), 7133-7150. doi:10.1175/Jcli-D-14-00034.1

Payne, A. E., & Magnusdottir, G. (2015). An evaluation of atmospheric rivers over the North Pacific in CMIP5 and their response to warming under RCP 8.5. *Journal of Geophysical Research-Atmospheres, 120*(21), 11173-11190. doi:10.1002/2015jd023586

Payne, A. E., & Magnusdottir, G. (2016). Persistent landfalling atmospheric rivers over the west coast of North America. *Journal of Geophysical Research-Atmospheres, 121*(22), 13287-13300. doi:10.1002/2016jd025549

Ralph, F. M., Coleman, T., Neiman, P. J., Zamora, R. J., & Dettinger, M. D. (2013). Observed Impacts of Duration and Seasonality of Atmospheric-River Landfalls on Soil Moisture and Runoff in Coastal Northern California. *Journal of Hydrometeorology, 14*(2), 443-459. doi:10.1175/Jhm-D-12-076.1

Ralph, F. M., & Dettinger, M. D. (2012). Historical and National Perspectives on Extreme West Coast Precipitation Associated with Atmospheric Rivers during December 2010. *Bulletin of the American Meteorological Society, 93*(6), 783-790. doi:10.1175/Bams-D-11-00188.1

Ralph, F. M., Neiman, P. J., Kiladis, G. N., Weickmann, K., & Reynolds, D. W. (2011). A Multiscale Observational Case Study of a Pacific Atmospheric River Exhibiting Tropical-Extratropical Connections and a Mesoscale Frontal Wave. *Monthly Weather Review, 139*(4), 1169-1189. doi:10.1175/2010mwr3596.1

Ralph, F. M., Neiman, P. J., Wick, G. A., Gutman, S. I., Dettinger, M. D., Cayan, D. R., & White, A. B. (2006). Flooding on California's Russian River: Role of atmospheric rivers. *Geophysical Research Letters, 33*(13). doi:Artn L1380110.1029/2006gl026689

Ralph, F. M., Rutz, J. J., Cordeira, J. M., Dettinger, M., Anderson, M., Reynolds, D., et al. (2019). A Scale to Characterize the Strength and Impacts of Atmospheric Rivers. *Bulletin of the American Meteorological Society, 0*(0), null. doi:10.1175/bams-d-18-0023.1

Rutz, J. J., Steenburgh, W. J., & Ralph, F. M. (2014). Climatological Characteristics of Atmospheric Rivers and Their Inland Penetration over the Western United States. *Monthly Weather Review, 142*(2), 905-921. doi:10.1175/Mwr-D-13-00168.1

Ryoo, J. M., Kaspi, Y., Waugh, D. W., Kiladis, G. N., Waliser, D. E., Fetzer, E. J., & Kim, J. (2013). Impact of Rossby Wave Breaking on U.S. West Coast Winter Precipitation during ENSO Events. *Journal of Climate, 26*(17), 6360-6382. doi:10.1175/Jcli-D-12-00297.1

Ryoo, J. M., Waliser, D. E., Waugh, D. W., Wong, S., Fetzer, E. J., & Fung, I. (2015). Classification of atmospheric river events on the US West Coast using a trajectory model. *Journal of Geophysical Research-Atmospheres, 120*(8), 3007-3028. doi:10.1002/2014jd022023

Sellars, S. L., Kawzenuk, B., Nguyen, P., Ralph, F. M., & Sorooshian, S. (2017). Genesis, Pathways, and Terminations of Intense Global Water Vapor Transport in Association with Large-Scale Climate Patterns. *Geophysical Research Letters, 44*(24), 12465-12475. doi:10.1002/2017gl075495

Shields, C. A., Rutz, J. J., Leung, L. Y., Ralph, F. M., Wehner, M., Kawzenuk, B., et al. (2018). Atmospheric River Tracking Method Intercomparison Project (ARTMIP): project goals and experimental design. *Geoscientific Model Development, 11*(6), 2455-2474. doi:10.5194/gmd-11-2455-2018

Sleator, D. D., & Tarjan, R. E. (1983). A Data Structure for Dynamic Trees. *Journal of Computer and System Sciences*, *26*(3), 362-391. doi:10.1016/0022-0000(83)90006-5

Smith, B. L., Yuter, S. E., Neiman, P. J., & Kingsmill, D. E. (2010). Water Vapor Fluxes and Orographic Precipitation over Northern California Associated with a Landfalling Atmospheric River. *Monthly Weather Review*, *138*(1), 74-100. doi:10.1175/2009mwr2939.1

Stan, C., Straus, D. M., Frederiksen, J. S., Lin, H., Maloney, E. D., & Schumacher, C. (2017). Review of Tropical-Extratropical Teleconnections on Intraseasonal Time Scales. *Reviews of Geophysics*, *55*(4), 902-937. doi:10.1002/2016rg000538

Tarjan, R. (1972). Depth-First Search and Linear Graph Algorithms. *SIAM Journal on Computing*, *1*(2), 146-160. doi:10.1137/0201010

Waliser, D. E., & Guan, B. (2017). Extreme winds and precipitation during landfall of atmospheric rivers. *Nature Geoscience*, *10*(3), 179-U183. doi:10.1038/Ngeo2894

Warner, M. D., Mass, C. F., & Salathe, E. P. (2015). Changes in Winter Atmospheric Rivers along the North American West Coast in CMIP5 Climate Models. *Journal of Hydrometeorology*, *16*(1), 118-128. doi:10.1175/Jhm-D-14-0080.1

Wick, G. A., Neiman, P. J., Ralph, F. M., & Hamill, T. M. (2013). Evaluation of Forecasts of the Water Vapor Signature of Atmospheric Rivers in Operational Numerical Weather Prediction Models. *Weather and Forecasting*, *28*(6), 1337-1352. doi:10.1175/Waf-D-13-00025.1

Xie, P. P., Yatagai, A., Chen, M. Y., Hayasaka, T., Fukushima, Y., Liu, C. M., & Yang, S. (2007). A Gauge-based analysis of daily precipitation over East Asia. *Journal of Hydrometeorology*, *8*(3), 607-626. doi:10.1175/Jhm583.1

Zhou, Y., Kim, H., & Guan, B. (2018). Life Cycle of Atmospheric Rivers: Identification and Climatological Characteristics. *Journal of Geophysical Research: Atmospheres*, *0*(ja). doi:10.1029/2018JD029180

Zhou, Y., & Kim, H. M. (2017). Prediction of atmospheric rivers over the North Pacific and its connection to ENSO in the North American multi-model ensemble (NMME). *Climate Dynamics*. doi:10.1007/s00382-017-3973-6

Zhu, Y., & Newell, R. E. (1994). Atmospheric Rivers and Bombs. *Geophysical Research Letters, 21*(18), 1999-2002. doi:10.1029/94gl01710

Zhu, Y., & Newell, R. E. (1998). A proposed algorithm for moisture fluxes from atmospheric rivers. *Monthly Weather Review, 126*(3), 725-735. doi:10.1175/1520-0493(1998)126<0725:Apafmf>2.0.Co;2